Received: 14 May 2021 | Revised: 26 July 2021 | Accepted: 28 July 2021

DOI: 10.1002/glia.24070

GLIA

WILEY

RESEARCH ARTICLE

Elucidating regulators of astrocytic Ca^{2+} signaling via multi-threshold event detection (MTED)

Franziska E. Müller[1] | Volodymyr Cherkas[1] | Gebhard Stopper[2] | Laura C. Caudal[2] | Laura Stopper[2] | Frank Kirchhoff[2] | Christian Henneberger[3,4,5] | Evgeni G. Ponimaskin[1] | Andre Zeug[1]

[1]Cellular Neurophysiology, Hannover Medical School, Hannover, Germany

[2]Department of Molecular Physiology, Center for Integrative Physiology and Molecular Medicine (CIPMM), University of Saarland, Homburg, Germany

[3]Institute of Cellular Neurosciences, Medical Faculty, University of Bonn, Bonn, Germany

[4]German Center for Neurodegenerative Diseases (DZNE), Bonn, Germany

[5]Institute of Neurology, University College London, London, UK

Correspondence
Andre Zeug, Cellular Neurophysiology, Hannover Medical School, Hannover, Germany.
Email: zeug.andre@mh-hannover.de

Funding information
Deutsche Forschungsgemeinschaft, Grant/Award Numbers: HE6949/1, HE6949/3, KI 503/12-2, PO732, SFB 894 A12, SFB1089 B03, SPP 1757, SPP1757, ZE994/2; Horizon 2020 Framework Programme, Grant/Award Number: 722053

Abstract

Recent achievements in indicator optimization and imaging techniques promote the advancement of functional imaging to decipher complex signaling processes in living cells, such as Ca^{2+} activity patterns. Astrocytes are important regulators of the brain network and well known for their highly complex morphology and spontaneous Ca^{2+} activity. However, the astrocyte community is lacking standardized methods to analyze and interpret Ca^{2+} activity recordings, hindering global comparisons. Here, we present a biophysically-based analytical concept for deciphering the complex spatio-temporal changes of Ca^{2+} biosensor fluorescence for understanding the underlying signaling mechanisms. We developed a pixel-based multi-threshold event detection (MTED) analysis of multidimensional data, which accounts for signal strength as an additional signaling dimension and provides the experimenter with a comprehensive toolbox for a differentiated and in-depth characterization of fluorescence signals. MTED was validated by analyzing astrocytic Ca^{2+} activity across Ca^{2+} indicators, imaging setups, and model systems from primary cell culture to awake, head-fixed mice. We identified extended Ca^{2+} activity at 25°C compared to 37°C physiological body temperature and dissected how neuronal activity shapes long-lasting astrocytic Ca^{2+} activity. Our MTED strategy, as a parameter-free approach, is easily transferrable to other fluorescent indicators and biosensors and embraces the additional dimensionality of signaling activity strength. It will also advance the definition of standardized procedures and parameters to improve comparability of research data and reports.

KEYWORDS
astrocyte, biosensor, Ca^{2+}, GCaMP, MTED

JEL CLASSIFICATION
C00; I29

Franziska E. Müller, Volodymyr Cherkas, and Gebhard Stopper contributed equally to this study

Evgeni G. Ponimaskin and Andre Zeug are equally contributing corresponding authors.

1 | INTRODUCTION

Fluorescence microscopy is a method used across many scientific disciplines. In biology, it allows researchers to visualize cellular processes in time and space largely preserving the integrity of the sample. Recent developments in novel microscopy techniques, biosensors, and indicators push functional imaging to its limits. A persistent major challenge is to adequately analyze multidimensional data. For example, Ca^{2+} is an important signaling molecule and, because of its large concentration gradients, a well-established readout for cellular activity. In some cell types, such as astrocytes, Ca^{2+} activity patterns can be very complex. Astrocytes are versatile glial cells participating in the maintenance of numerous brain functions, including the regulation of ion homeostasis, neurotransmitter clearance, energy supply, and blood flow (Sofroniew & Vinters, 2010). They are a crucial element in the brain architecture and display very distinct morphological characteristics that vary between brain regions and sub-regional networks (Chai et al., 2017). With their fine processes, astrocytes contact synapses. As active partners at the tripartite synapse, they release gliotransmitters that regulate synaptic activity (Araque et al., 2014; Bonansco et al., 2011; Henneberger et al., 2010; Panatier et al., 2011). In return, the release of a variety of neurotransmitters has been shown to modulate the cytosolic Ca^{2+} concentration ($[Ca^{2+}]$) in astrocytes (Porter & Mccarthy, 1997). Variations in astrocyte $[Ca^{2+}]$ have been proposed to represent a unique manner of cellular signaling, but revealing the exact functions and regulatory mechanisms remains a challenge (Semyanov et al., 2020; Volterra & Meldolesi, 2005). Ca^{2+} signals in astrocytes are not solely stimulus-dependent, but also occur spontaneously (Nett et al., 2002). They can also propagate and fuse, thus creating complex spatiotemporal patterns of activity. Whether these diverse patterns in Ca^{2+} activity correlate with distinct astrocytic functions and morphological features is a matter of extensive debate.

Ca^{2+} activity in astrocytes appears as local and very distinct fluctuations but could also spread into distant regions or engage the whole cell. Therefore, the spatial extent and amplitude of Ca^{2+} events are additional measures and standard evaluation approaches used in other applications cannot simply be transferred to astrocytic Ca^{2+} activity (Volterra et al., 2014).

A standard approach to analyzing Ca^{2+} activity is fluorescence microscopy using Ca^{2+} sensitive fluorescent dyes (Meldolesi, 2004). They generally come in two flavors: organic dyes, such as Oregon Green 488 BAPTA-1 (OGB-1), and genetically encoded Ca^{2+} indicators (GECIs), such as GCaMPs, which both have their specific advantages and disadvantages (Chen et al., 2013; Semyanov et al., 2020). Both are easy to use in single channel recordings, which simplifies the readout and subsequent data processing (Horikawa, 2015; Pérez Koldenkova & Nagai, 2013). Various tools are available to extract relative changes in $[Ca^{2+}]$, which mainly analyze the frequency and amplitude of events (Venugopal et al., 2019) based on predefined or automatically detected active regions (Agarwal et al., 2017; Castro et al., 2011). Recently, alternative approaches have been presented that also analyze the directionality of propagating events and the origin of Ca^{2+} events, which is predominantly located in the fine peripheral processes (Wang et al., 2019; Wu et al., 2014, 2019). This has shifted the focus from major Ca^{2+} changes in the somatic region to the periphery. However, these regions provide only a weak fluorescent signal due to their low volume. Therefore, when the detection method is based on identifying signals above noise level, events in these areas can escape detection due to a low signal-to-noise-ratio.

We developed a strategy to determine the fluorescence signal of Ca^{2+} indicators at a basal $[Ca^{2+}]$, F_0, which was the basis for calculating $(F-F_0)/F_0$, expressed as $\Delta F/F_0$, as a measure of relative changes in $[Ca^{2+}]$ in a pixel-based manner. We then applied an automated multi-threshold event detection (MTED) algorithm to quantify the intrinsic Ca^{2+} activity of astrocytes in primary hippocampal cultures, organotypic slice cultures, and cortical astrocytes in vivo. This allows to combine the information of amplitude and spatial extend over time to investigate the magnitude of Ca^{2+} events as a measure of signaling strength. Next, we tested MTED in two straightforward experimental settings. We could demonstrate substantially different Ca^{2+} activity dynamics of cultured astrocytes at room temperature (RT) compared to 37°C, which resembled the activity measured in vivo. We could further reveal that neuronal activity favors the generation of long-lasting $[Ca^{2+}]$ elevations in astrocytes. Our flexible MTED algorithm, exploited here successfully for Ca^{2+} indicators and astrocyte physiology across preparations in 2D over time, is easily applicable to investigate functional dynamics using various fluorescence-based indicators and biosensors and can be easily extended to 3D over time and to other cell types.

2 | MATERIAL AND METHODS

2.1 | Animals for in vitro Ca^{2+} imaging

For all in vitro experiments, wildtype animals of both genders from strain C57BL/6J were used. Animals were housed and cared for in accordance to directive 2010/63/EU. Mice were kept in a 14 h light and 10 h dark cycle with lights on starting at 7 am. Animals had *ad libitum* access to food and water and were kept under standard conditions at 22 ± 2°C RT with 55% ± 5% humidity. Mice were killed by decapitation, and all experiments were conducted according to the recommendations of the European commission and Lower Saxony's "Landesamt für Verbraucherschutz und Lebensmittelsicherheit" (authorization number 2018/179).

2.2 | Animals for in vivo Ca^{2+} imaging

Mice were maintained in the animal facility of the Center for Integrative Physiology and Molecular Medicine (CIPMM, University of Saarland). Astrocyte-specific knock-in GLAST-CreERT2 mice (Slc1a3tm1 [cre/ERT2]Mgoe, MGI:3830051) (Mori et al., 2006) were crossbred to Rosa26 reporter mice with GCaMP3 expression (Gt(ROSA)26Sortm1 (CAG-GCaMP3)Dbe, MGI: 5659933) (Paukert et al., 2014). Imaging sessions were performed at 8–10 weeks of age. Mouse administration was managed via the PyRAT database (Python based Relational Animal Tracking) from Scionics Computer Innovation GmbH (Dresden, Germany). Animals were kept and bred in strict accordance with the

recommendations to European and German guidelines for the welfare of experimental animals. Animal experiments were approved by the Saarland state's "Landesamt für Gesundheit und Verbraucherschutz" in Saarbrücken/Germany (license numbers: 71/2013 and 36/2016).

2.3 | Primary hippocampal astrocyte cultures

Primary astrocyte cell cultures were prepared according to a previously described protocol (Wu et al., 2014) with slight modifications: Hippocampi were isolated from brains of neonatal mice between P1-3 and cells were seeded after dissociation at a density of 5×10^4 cells per 12 mm glass coverslip for microscopy in 500 μL plating medium (49 mL MEM, 1 mL B-27 supplement, 500 μL sodium pyruvate, 500 μL L-Glutamine, 50 μL Penicillin–Streptomycin; all Thermo Fisher Scientific Inc., Waltham). On DIV3 the entire plating medium was replaced with 1 mL maintenance medium (49 mL Neurobasal-A, 1 mL B-27 supplement, 500 μL L-Glutamine, 50 μL Penicillin–Streptomycin; all Thermo Fisher Scientific Inc., Waltham). On DIV11, ½ of the medium was exchanged with prewarmed maintenance medium prior to infection of the cells with of 0.1 μL AAV-mGFAP-GCaMP6s (3.7×10^9 vg/μL) and AAV-mGFAP-tdTomato (1×10^7 vg/μL). Astrocytes were maintained at 37°C in a humidified incubator in a 5% CO_2 atmosphere used for experiments between DIV14-17. Cells were transferred to a prewarmed recording chamber for microscopy and kept in a balanced salt solution (BSS), which was adjusted to pH 7.4 and 290 mOsm with glucose, containing 115 mM NaCl, 5.4 mM KCl, 1 mM $MgCl_2$, 2 mM $CaCl_2$ and 20 mM HEPES.

2.4 | Organotypic slice cultures

Organotypic slice cultures were prepared after an adapted protocol from Kobe et al. (Kobe et al., 2012). Briefly, mice were decapitated at P6 under sterile conditions and the isolated hippocampus was placed in ice-cold oxygenized slice medium in a 60 mm dish for 30 min. 350 μm thick slices were prepared with McIlwain Tissue Chopper (Mickle, Surrey, UK) and separated with a needle to select 2–4 slices with complete hippocampal structures. Selected slices were transferred onto Millicell filter inserts (#PICM03050, Merck, Darmstadt, Germany) in a 6-well plate containing 1 mL slice maintenance medium (50% MEM, 25% Hanks' balanced salt solution, 25% horse serum, and 2 mM glutamine at pH 7.3). Excess liquid around the slice was removed and cells were subsequently infected by application of 0.2 μL AAV-mGFAP-GCaMP6s (3.7×10^9 vg/μL) into the medium. Slices were kept in a humidified atmosphere (5% CO_2, 37°C) with ½ of the medium being exchanged on DIV2, DIV4 and DIV6. Ca^{2+} imaging was conducted at DIV5-7.

2.5 | Cranial window surgery for in vivo two-photon imaging

During surgical procedures, animals were kept on heating pads and eyes were covered with Bepanthen ointment (Bayer, Leverkusen, Germany). Anesthesia was induced with a mixture of 5% isoflurane, 47.5% O_2 (0.6 L/min) and 47.5% N_2O (0.4 L/min) and maintained with 2% isoflurane (Harvard Apparatus anesthetic vaporizer, Harvard, Holliston). A standard craniotomy (Cupido et al., 2014) of 3 mm in diameter was performed over the somatosensory cortex (2 mm posterior and 1.5 mm lateral to bregma). The craniotomy was sealed with a glass coverslip (Glaswarenfabrik Karl Hecht, Sondheim, Germany; #1.5 thickness code) and fixed with dental cement (RelyX®, 3 M ESPE, Seefeld, Germany). Subsequently, a metal holder for head restraining (5 mm diameter) was applied and fixed to the skull with dental cement. After surgery, the animals were kept on the heating pad until complete recovery. Post-operative treatment consisted of buprenorphine (3 mg/kg, s.c.) and dexamethasone (0.2 mg/kg, i.p.), for three consecutive days. Recovery was assessed by body weight and mouse grimace scale. After five to seven days the first imaging session was performed.

In preparation for Ca^{2+} imaging, animals were habituated before the first imaging session according to adapted protocols without water restriction from Guo et al. (Guo et al., 2014) and Kislin et al. (Kislin et al., 2014) The animals were head-fixed with a custom-designed head-restrainer, 3D-printed using stainless steel. During imaging, anesthesia was applied using a custom-made, magnetically attachable anesthesia mask. Each field of view (FOV) was imaged twice: first in anesthetized, then in awake state. During imaging in anesthetized state, isoflurane concentration was kept at 1.5%, and flow of O_2 and N_2O was set to 0.6 and 0.4 L/min, respectively. Before awake state imaging, isoflurane and other gasses were switched off and it was verified that the animals were fully awake. The selected FOVs for Ca^{2+} imaging were located in the somatosensory cortex, 80–100 μm beneath the dura. Each FOV was recorded for 5 min to investigate the Ca^{2+} signals. The total duration of one imaging session ranged between 30 and 60 min per animal. After imaging, animals were kept on a heating pad at 37°C until they recovered completely, additionally Fresubin (Fresenius Kabi, Bad Homburg, Germany) was provided *ad libitum*.

2.6 | Reagents

Tetrodotoxin citrate (TTX; #Asc-055; Ascent Scientific, Princeton, NJ) was used at a concentration of 10 nM to block neuronal activity and was applied several minutes prior to imaging. The Ca^{2+}-ATPase inhibitor Cyclopiazonic acid (CPA; #120300, Abcam, Cambridge, UK) was applied at a concentration of 10 μM at least 10 min before the measurements.

2.7 | Microscopy

Ca^{2+} imaging in vitro and in situ was conducted on an upright Andor Spinning Disk microscope (Oxford Instruments, Belfast, Northern Ireland) equipped with a CSU-X1 (Yokogawa, Musashino, Japan) using filter cubes (537/26 nm) for full frame imaging of GCaMP6s or split filter cubes (609/54) for simultaneous imaging of GCaMP6s and tdTomato. Cells were recorded for 10 min with 5 frames/s using

excitation wavelength 488 nm (GCaMP6s) and 561 nm (tdTomato). The temperature of the BSS for measurement was controlled by a custom-built heating device and additionally supervised with an external thermometer. To achieve thermal stability and avoid artifacts during recordings the objective, stage and chamber were all heated to the desired temperature.

In vivo Ca^{2+} imaging was conducted in anaesthetized (1.5% isoflurane) and awake head-fixed mice through a cortical cranial window in the prefrontal cortex using two-photon excitation laser scanning microscopy (TPE-LSM). The custom-built microscope was equipped with a resonant scanner (RESSCAN-MOM, Sutter instrument, Novato) and a 20x water-immersion objective (W Plan-Apochromat 20x/1.0 DIC D = 0.17; Zeiss, Jena, Germany). Images were acquired with a frame rate of 30 Hz and a 10 Hz frame-averaging factor, resulting in an effective acquisition rate of 3 Hz. To minimize photo-damage, the excitation laser power was kept at a minimum for a sufficient signal-to-noise ratio (<40 mW at 60 ns pixel dwell time). Laser wavelength was set to 890 nm (Chameleon Ultra II, Ti:Sapphire Laser; Coherent, Santa Clara). The emitted light was detected by a photomultiplier tube (R6357; Hamamatsu, Hamamatsu, Japan) and pre-amplified (DHPCA-100, Femto, Berlin, Germany). Digitizer (NI-5734) and control hardware (NI-6341) was housed in a PXIe (1082) chassis, connected to a control-PC via a high bandwidth PXIe-PCIe8398 interface (NI, Austin). Scanning and image acquisition were controlled by ScanImage (SI 5.6R1) (Pologruto et al., 2003).

2.8 | Data processing

Data were processed using Matlab. In vitro data obtained by confocal spinning disk microscopy were denoised using VBM3D (Maggioni et al., 2012) and low intensity TPE-LSM data by SURE-LET. An automated data offset control was obtained by analyzing the data intensity histogram. The F_0 calculation is based on 'moving window' filter functions, where the mean and variance of F are used as weighting functions for F to identify low intensities. The 'moving window' sizes for filtering are input parameters, dependent on acquisition settings and the temporal profile of expected signal changes. The MTED algorithm uses F_0 or F_R, the fluorescence signal of an equally expressed reference fluorescent protein (FP), and applied various Ca^{2+} thresholds to $\Delta F/F_0$ or $\Delta F/F_R$, respectively. To reject false-positive pixels, we applied an appropriate F_0 threshold to eliminate background signals, such as readout noise. Next, basic morphological gray-scale operations (opening and closing) were performed to close holes and remove small isolated peaks, followed by Gaussian smoothing of the Ca^{2+} signals. This was used as a weighting function. Groups of Ca^{2+}-positive regions were then identified based on their spatio-temporal connectivity. Small groups not exhibiting a minimum size and duration were rejected. The time dependence of a detected event was stored for visualization and further analysis. The Ca^{2+} event detection was repeated for various Ca^{2+} thresholds. For practical reasons, we use logarithmic-like spaced threshold levels, such as [0.2, 0.5, 1, 2, 5, 10] fold change in F.

2.9 | Statistical analysis

Data were analyzed for statistical significance using GraphPad Prism 8. The individual statistical tests are indicated in the respective figure legends.

2.10 | Data and materials availability

The Matlab code developed in this study is available from the corresponding author upon request.

3 | RESULTS

3.1 | Visualization of Ca^{2+} transients in astrocytes

For developing a strategy to accurately characterize Ca^{2+} activity, we used primary cultures of mouse hippocampal astrocytes expressing the Ca^{2+} indicator GCaMP6s. These cells exhibit extensive endogenous Ca^{2+} activity with varying amplitudes and magnitudes, changing directionality and regional patterns (Figure 1, Movie S1). The GCaMP6s fluorescence signal F is sensitive to changes in Ca^{2+} levels, but also depends on the indicator concentration itself and the cellular structure, which determines the number of molecules in the focal volume. Figure 1 shows an example of Ca^{2+} changes in cultured hippocampal astrocytes. From the GCaMP6s fluorescence signal F (Figure 1(a) and Supplementary Figure S1(a)), which scales with both the Ca^{2+} and GCaMP concentration, it is not possible to deduce the changes in $[Ca^{2+}]$ directly. The time series shown in Figure 1(b) contains various regions presenting similar brightness at some points over time (regions of interest [ROIs] 1–4). While the intensity of ROI 4 stays constant over time, F in ROIs 1–3 varies and can be identified as changes in Ca^{2+} levels. To obtain a quantity, which is independent from the indicator concentration and the number of indicator molecules in the focal volume, we developed an automated pixel-based calculation of F_0 derived from the indicator signal F (Supplementary Figure S2 and Movie S2). F_0, deduced from the temporal behavior of F, represents the indicator signal at lowest $[Ca^{2+}]$. The resulting $\Delta F/F_0$ provides an indicator concentration-independent readout which reflects relative changes in $[Ca^{2+}]$ (Figure 1(c),(e), Movie S1). Alternatively, cytosolic co-expression of a Ca^{2+}-insensitive FP (e.g., tdTomato) as a reference probe (F_R) can be used to account for pixel and time dependent differences in the number of indicator molecules in the focal volume (compare Supplementary Figure S1 and Movie S1). A common strategy of detecting Ca^{2+} events from F is based on identifying signals above noise level (often a factor times the standard deviation of F). This can be a source of biases because only very pronounced changes in Ca^{2+} exceed the noise level at small, peripheral structures, where F is small as well (see Supplementary Figure S2). We can further visualize the spatiotemporal increases and decreases in cytosolic Ca^{2+} $(d(\Delta F/F_0)/dt)$, depicted as red and blue regions, respectively, in Figure 1(d) and Movie S1(d).

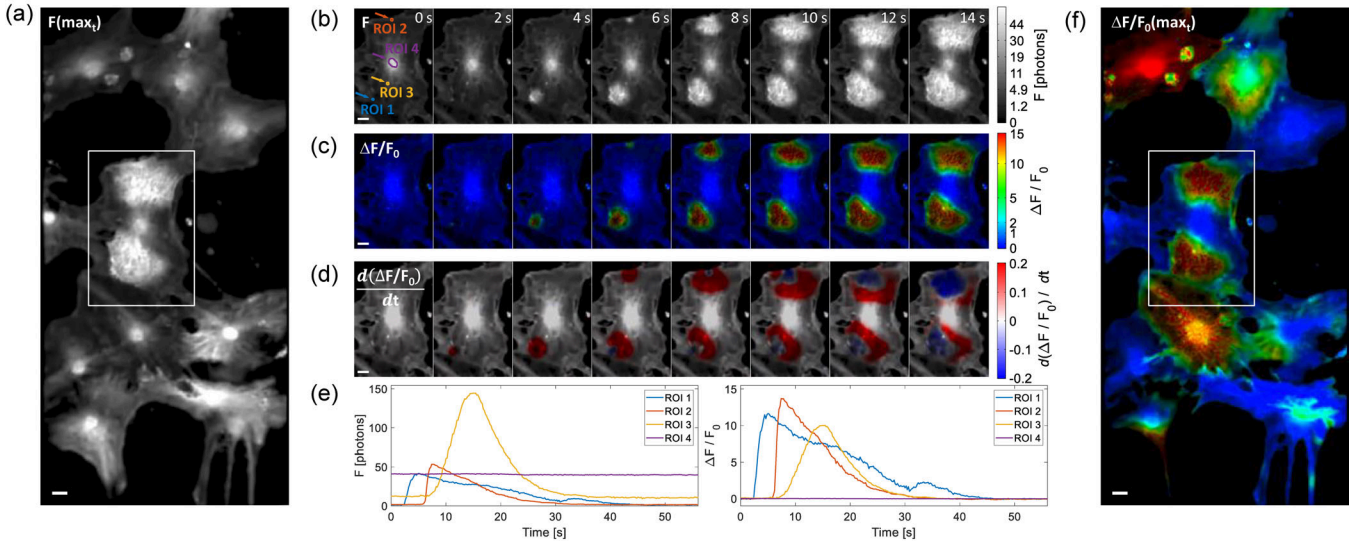

FIGURE 1 Visualization of Ca^{2+} activity using intensity-based indicators. (a) Maximum fluorescence signal F (F(max$_t$)) of Ca^{2+} indicator GCaMP6s in a 14 s sequence of a 10 min recording of primary mouse hippocampal astrocytes. Scale bar = 10 μm. (b) Propagation of Ca^{2+} activity reflected by increased F intensity in the zoom region (white box in a). Various regions of interest (ROIs) show similar brightness at a given time point due to the GCaMP content in the confocal volume, but only those with changing Ca^{2+} levels vary in brightness over time (compare ROIs 1–3 with ROI 4). Scale bar = 10 μm. (c) Application of $\Delta F/F_0$ by scaling F to lowest Ca^{2+} presence deduced from its temporal behavior to cancel out differences in F due to different number of indicator molecules in the focal volume. (d) the color-coded amplitude of changes in Ca^{2+} levels as $d(\Delta F/F_0)/dt$, with red colors indicating an increase in Ca^{2+} and blue colors representing decreasing Ca^{2+}. (e) Time trace of the selected ROIs shown in (b), with dissimilar properties and different changes in F over time (compare (b),(c)), obtained by the described approaches in (b),(c). (f) Counterpart to (a) showing $\Delta F/F_0(max_t)$, which revealed profound spatial differences in detected Ca^{2+} activity

Comparison of the overview images in Figure 1(a),(f), where the maximum projection of a 15 s time window is shown as intensity F and as false color $\Delta F/F_0$, respectively, underlines the benefit of the ratiometric concept. Bright regions, like some cell somata in Figure 1(a), are characterized by low changes in Ca^{2+}, whereas others exhibit high Ca^{2+} activity.

3.2 | Multi-threshold event detection

The analysis of Ca^{2+} activity in astrocytes should provide detailed information on event duration, size, and magnitude (see Figure 1, Movie S1). A fundamental question is: which changes in Ca^{2+} can be called a Ca^{2+} event? Furthermore, differences in the characteristics of Ca^{2+} events need to be identified and should be reported by an event detection algorithm. Such an algorithm should also capture the spatial extent of the events without prior definition of static ROIs. Furthermore, the detection algorithm should not require experiment-specific settings. Therefore, we developed MTED, a pixel-based, dynamic event detection algorithm relying on multiple thresholds, which computes the abovementioned variables (Figure 2(a),(b), Movie S3). Condition-specific adjustments of parameters are not required.

Through Monte Carlo simulations, we found that the accuracy in identifying a pixel above a specific Ca^{2+} threshold can be far below 95% confidence and varies with F_0 (see Supplementary Figure S2). We selected a set of six thresholds (0.2, 0.5, 1, 2, 5, 10) expressed in terms of $\Delta F/F_0$, where a Ca^{2+} event reaching a threshold of 0.2 or 1 does not necessarily reflect a 20% or double increase in basal Ca^{2+} concentration, respectively (see Semyanov et al., 2020). In conjunction with proximity relationships of neighboring pixels (xyt), MTED identifies groups of Ca^{2+}-positive pixels for a set of Ca^{2+} thresholds, thereby allowing for dynamic region changes. The output for the sequence shown in Figure 1(c) is shown in Figure 2(c) and Movie S3. Here, the six Ca^{2+} thresholds applied are depicted as contour lines with different colors, which show the respective spatial signal dynamics. A statistical analysis of the complete dataset is shown in Figure 2 (d) as frequency plots for all analyzed Ca^{2+} thresholds exemplifying the maximum size of the events, their duration, and the maximum distance of the event center traveled over time (see Supplementary Figure S3 for more statistical parameters). The frequency plots shown in Figure 2(d) can be accumulated for different experimental conditions and be compared as shown below. Overall, the MTED algorithm provides a comprehensive analysis of spatiotemporally complex fluorescence changes.

3.3 | The temperature-dependence of Ca^{2+} event characteristics

We next applied the analysis to two physiologically meaningful experimental scenarios. Investigations with cultured astrocytes are often carried out at RT (i.e., ~ 25°C) rather than at the physiological body temperature (i.e., 37°C). When investigating Ca^{2+} event characteristics of the same astrocytic culture at different environmental temperatures, we observed substantial differences in the Ca^{2+} activity

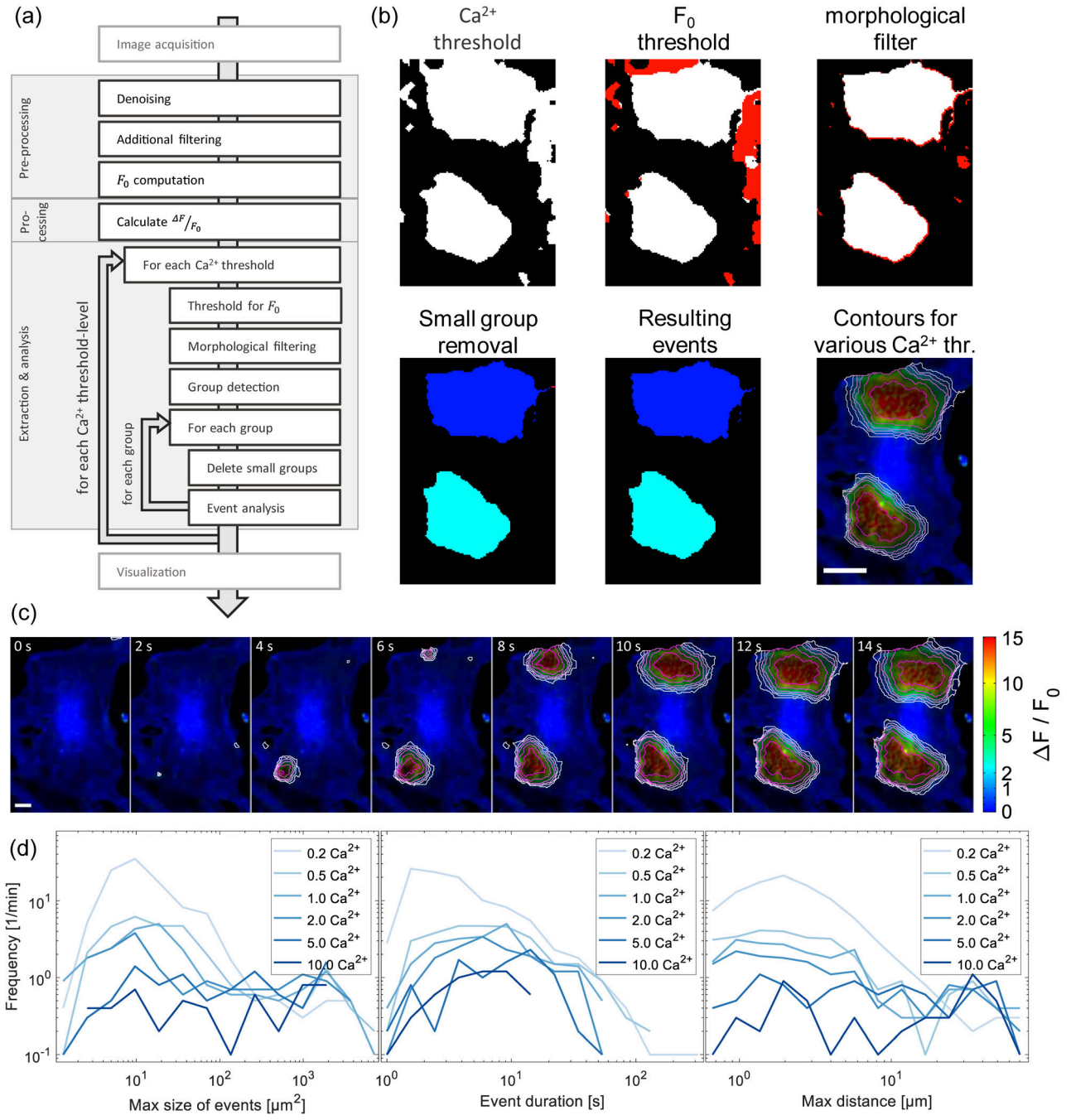

FIGURE 2 Data processing and Ca^{2+} event detection workflow. (a) Diagram of steps in the evaluation process: image acquisition, data preprocessing, including a novel approach for a pixel-based F_0 calculation, Ca^{2+} fluctuation recognition, $\Delta F/F_0$ and the multi-threshold approach for event detection (MTED), and the final activity visualization. (b) Representative images of the main steps in the data processing workflow depicted in (a). The red pixels depict regions removed from the previous step. Scale bar = 20 µm. (c) Visualization of Ca^{2+} events calculated from the zoom region in Figure 1 and shown for various thresholds from Ca^{2+} = 0.2, 0.5, 1, 2, 5, 10 (white to magenta). Scale bar = 10 µm. (d) Main output characteristics of the Ca^{2+} activity analysis: maximum size of detected events (lateral extent, x,y), mean event duration (t), and maximum distance the area center traveled within the event (µm)

patterns (Figure 3, Movie S4). Figure 3(a) illustrates the Ca^{2+} events detected within the zoomed-in region shown in Figure 1(b)–(e) for 25, 34, and 37°C. At 25°C, both events (ROI 1 and 2 from Figure 1) slowly increased, reaching large areas and high amplitudes. At 34°C, events in nearby regions were much shorter and occupied much smaller areas. At 37°C, the detected events that originated from the same initial region were spatially restricted and shorter. Such temperature-dependent changes become more obvious when illustrated in 3D (Figure 3(b), Movie S5). Statistical analysis of the maximum event size, event duration, and maximum distance of event propagation revealed that at 25°C strong Ca^{2+} changes up to 10-fold were detected, spanning over the complete parameter range for the

maximal size and distance of Ca^{2+} events (Figure 3(c), Supplementary Figure S3, Movie S5). At 34°C, high-magnitude Ca^{2+} events were still detected but overall smaller magnitudes became more frequent. At 37°C, high Ca^{2+} levels were not reached any longer and small-magnitude Ca^{2+} events dominated. Event duration and maximum propagation distance also display a clear temperature dependence such that Ca^{2+} events become shorter and propagated less at higher temperature.

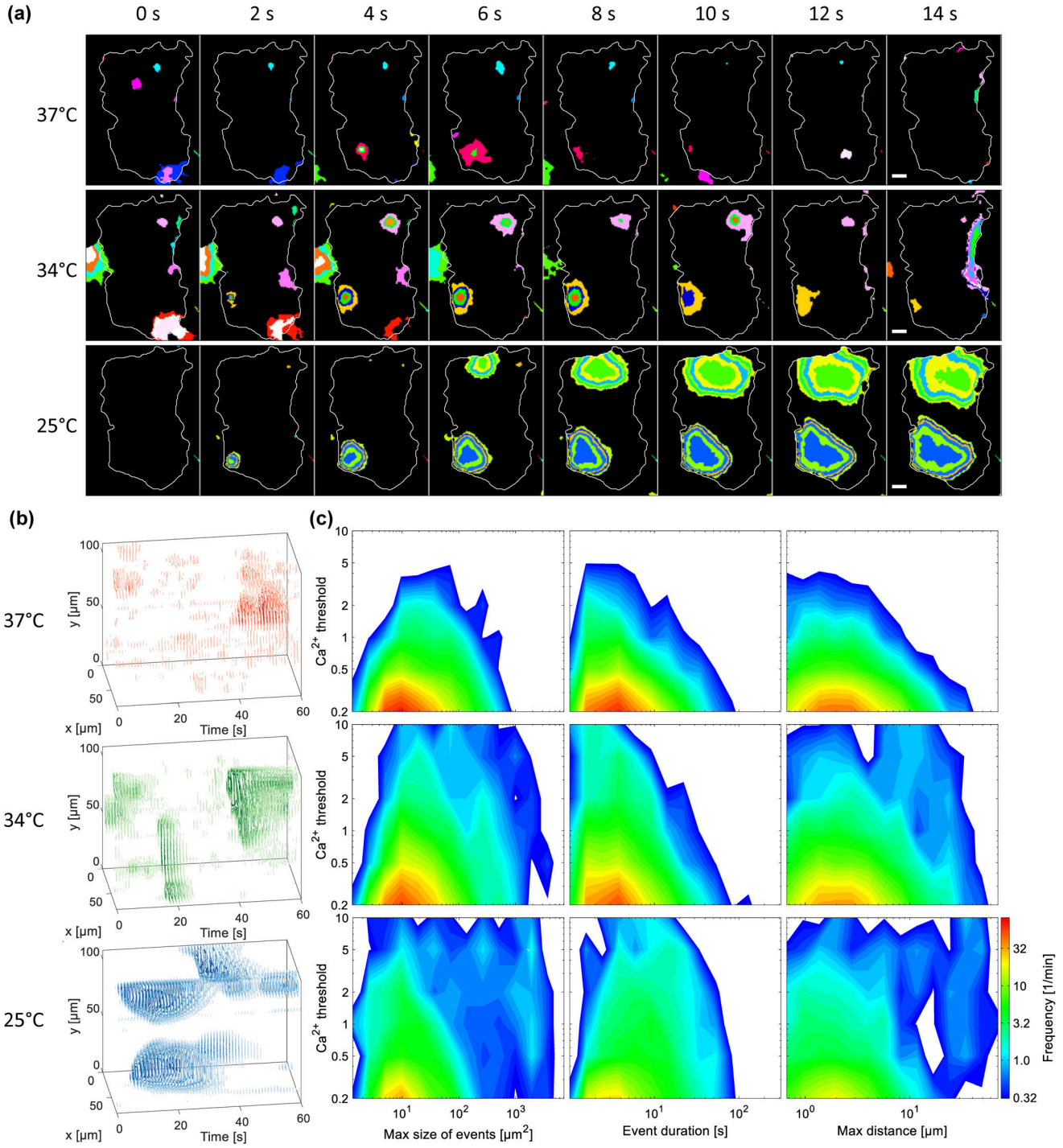

FIGURE 3 Astrocytic Ca^{2+} event characteristics are shaped by ambient temperature. (a) Comparison of Ca^{2+} activity detected in the same cell at 37°C, 34°C, and 25°C for a sequence of 14 s color-coded for various thresholds. Data were captured in a time sequence of 10 min at 25°C, the sample heated to 34°C, and a sequence acquired from the same region. The measurement was repeated at 37°C and the sample cooled back to 34°C and then to 25°C (see Movie S4). Scale bar = 20 µm. (b) 3D contour plots of detected events, with darker colors representing higher changes in Ca^{2+}, illustrating the change in Ca^{2+} activity with environmental temperatures. (c) 2D histograms as a statistical presentation of selected parameters. At 37°C, the detected events are very small in space, transient in time, and do not reach high magnitudes. These characteristics change with cooler environments, reaching longer lasting, spatially more extensive, and comparably high magnitude events during measurement at 25°C

3.4 | Suppression of cytosolic Ca^{2+} clearance reproduces the low temperature pattern

To understand the mechanisms underlying the observed temperature-dependent differences in the Ca^{2+} patterns, we compared the maximum increase and decrease in the Ca^{2+} signal, $\max_t(d(\Delta F/F_0)/dt)$ and $\min_t(d(\Delta F/F_0)/dt)$, respectively, for each detected Ca^{2+} event (Figure 4(a)). At 37°C, the signal increases were very local with low amplitude. In contrast, regions with positive changes in Ca^{2+} were spread over wider areas and reached greater amplitudes at lower temperatures. Similarly, the decrease in Ca^{2+} overlaying centers of maximal increase was punctual at 37°C but spread over wider regions at lower temperatures. Overall, negative Ca^{2+} changes were substantially greater at 34°C than 25°C. The rate of positive and negative Ca^{2+} changes was similar at 37°C, the positive Ca^{2+} changes (i.e., spreading of events) overcame the negative changes (i.e., depletion of events) at 25°C (Figure 4(b)).

Next, we used this analysis to investigate what underlies the profoundly different Ca^{2+} characteristics. The decrease in Ca^{2+} levels reflects its removal from the cytosol, for instance into the endoplasmic reticulum (ER). The latter depends to a significant degree on Ca^{2+} pumps localized in the ER membrane (sarco/ER Ca^{2+} ATPases; SERCA pumps). Therefore, their inhibition should strongly affect Ca^{2+} activity patterns. Pharmacological inhibition of SERCA pumps by cyclopiazonic acid (CPA, 10 μM) strongly prolonged Ca^{2+} transients. The results obtained from these experiments suggest that a temperature-dependent slowdown of Ca^{2+} extrusion from the cytosol could explain the differences in the observed Ca^{2+} activity patterns (Figure 4(c),(d)). Notably, lowering the temperature only partially slows down ATP-driven Ca^{2+} uptake processes, whereas CPA blocks ATP-driven Ca^{2+} uptake to a greater extent. As in Figure 4(b), analyses of the ratio of maximal positive to negative temporal Ca^{2+} changes were performed for each pixel of an event (Supplementary Figure S4). At low temperatures, the uptake is substantially blocked homogeneously throughout the cells. Overall, the MTED analysis presented here successfully captured complex signaling patterns and enabled us to compare them between experiments.

3.5 | Event characteristics in situ

We next analyzed astrocytic Ca^{2+} events in organotypic slice cultures from the mouse hippocampus. In such preparations, the morphological

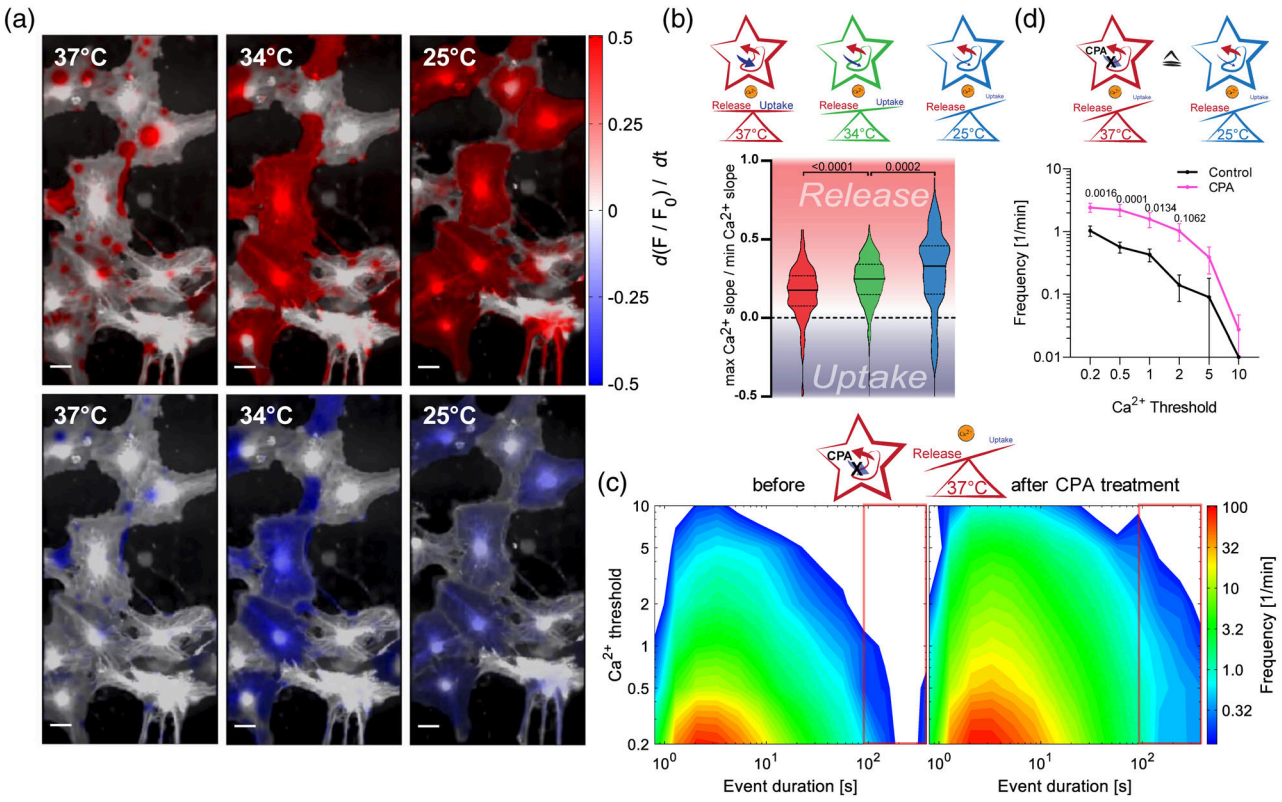

FIGURE 4 Slow physiological processes account for extended Ca^{2+} events at low temperatures. (a) Visualized maximum increase $\max_t(d(\Delta F/F_0)/dt)$ and decrease $\min_t(d(\Delta F/F_0)/dt)$ of the Ca^{2+} signal reveals distinct behavior at the given temperatures. Scale bar = 20 μm. (b) Ratio of the maximum and minimum Ca^{2+} change of all detected events in the measurements of the three investigated temperatures. For all Ca^{2+} thresholds, threshold 1 is shown, and the ratio reveals the discrepancy of Ca^{2+} release to its uptake velocity, which is increased at 25°C compared to 34°C and 37°C. (c) 2D histograms of Ca^{2+} event duration at 37°C before and after incubation with Ca^{2+}-ATPase inhibitor CPA. Pharmacological blockage of Ca^{2+} uptake led to similar event characteristics as obtained at low temperatures ($n = 10$, $N = 3$). (d) Statistical evaluation of Ca^{2+} activity with duration >90 s as a function of the Ca^{2+} threshold applied in the MTED algorithm. Data show mean and SEM. Two-way ANOVA with Sidak's multiple comparisons post-hoc test

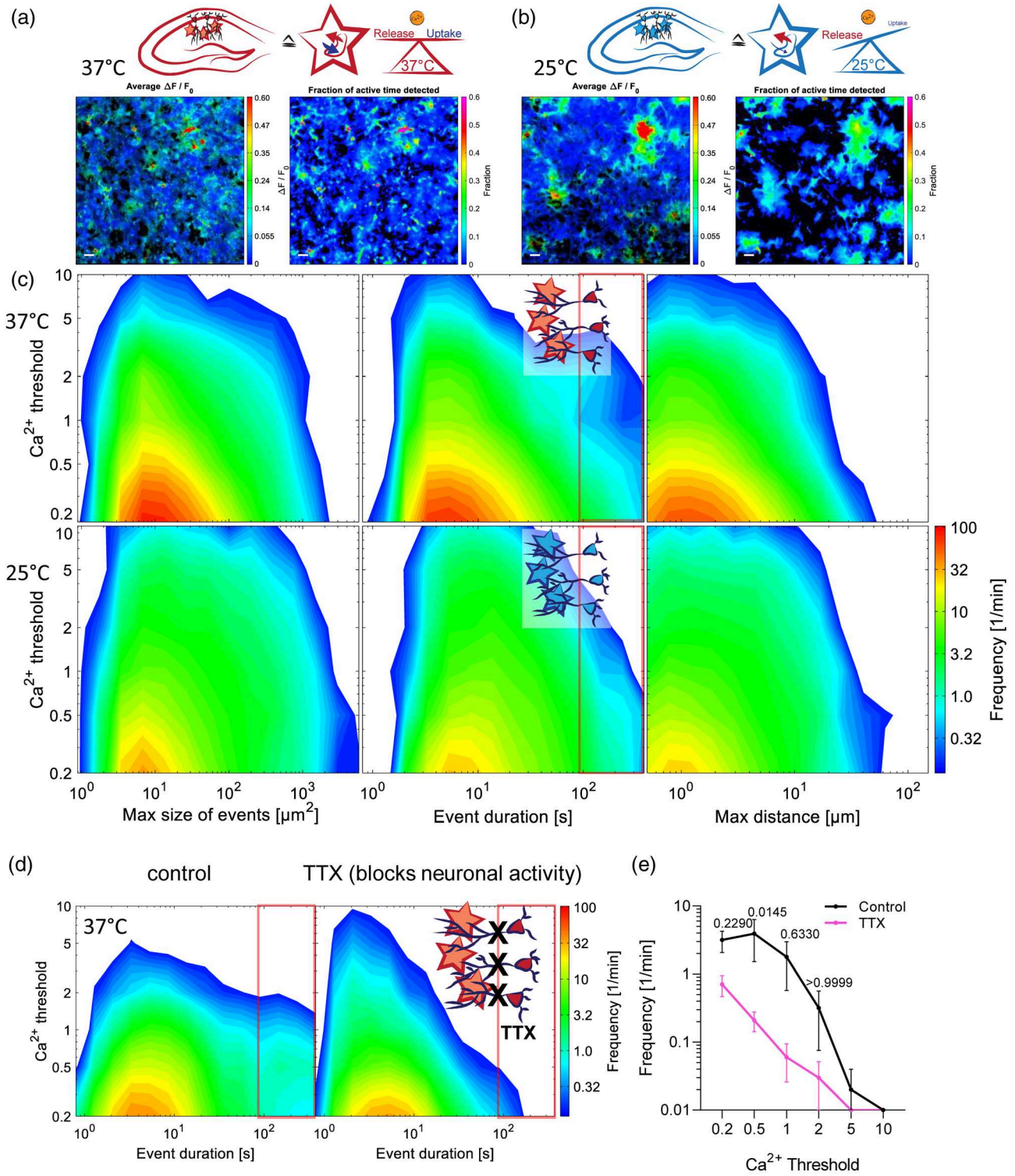

FIGURE 5 Temperature phenotype of Ca^{2+} activity is not restricted to primary astrocyte cultures. (a),(b) Average $\Delta F/F_0$ (left images) and the fraction of active time, which is the relative time for each pixel above a Ca^{2+} threshold of 0.2 (right images), detected in organotypic hippocampal slice cultures at 37°C (a) and 25°C (b). Comparably higher $\Delta F/F_0$ with spatially more extended and longer lasting events was detected at 25°C, similar to primary astrocyte cultures. Scale bars = 20 µm. (c) 2D histograms of the selected parameters maximum size, duration, and traveled distance of events characteristic for organotypic slice cultures incubated at 37°C, and 25°C incubation temperature depict similar changes in features as observed in primary cultures ($n = 6$ for 37°C and $n = 5$ for 25°C from $N = 3$ independent cultures). (d) Averaged 2D histogram of control measurements in organotypic slice cultures showing prolonged event duration at 37°C compared to primary astrocyte cultures (red framed area, left panel). Blocking the neuronal activity with TTX reduces the occurrence of long-lasting Ca^{2+} events and exhibits similar 2D histogram features as primary astrocyte cultures at 37°C. (e) Statistical evaluation of Ca^{2+} activity with duration >90 s (red framed area in (d)) as a function of the Ca^{2+} threshold applied in the MTED algorithm. Data show mean and SEM. Two-way ANOVA with Sidak's multiple comparisons post-hoc test ($n = 10$ recordings from $N = 3$ experiment days in (d) and (e))

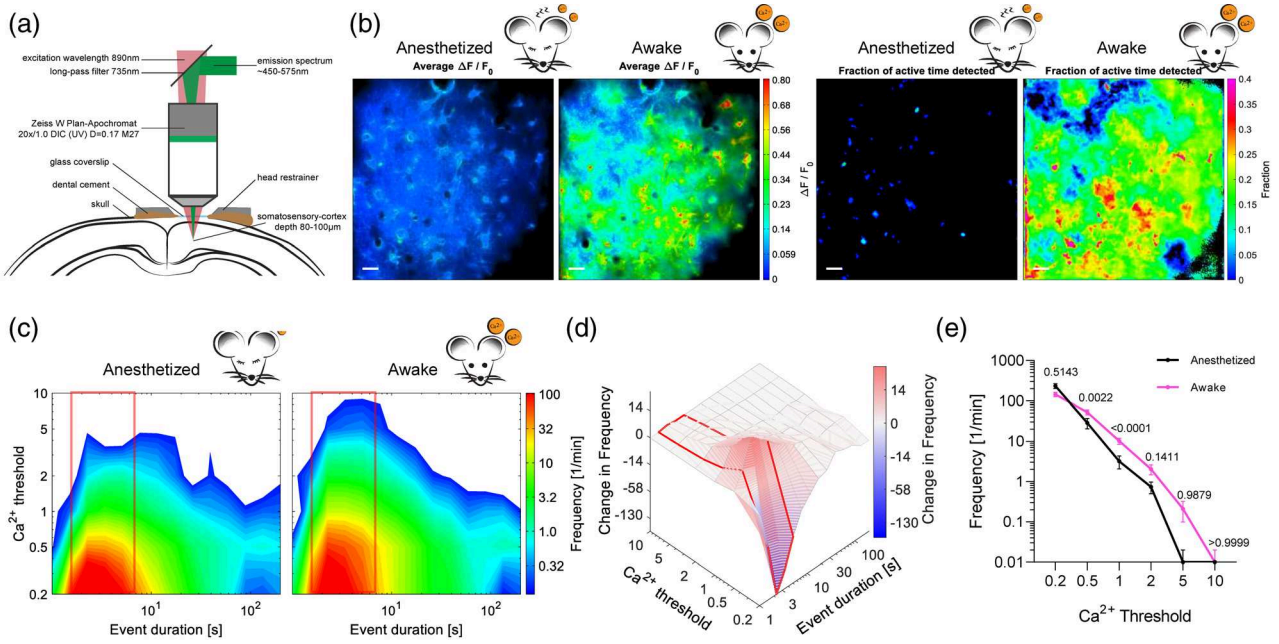

FIGURE 6 Ca^{2+} event detection strategy MTED is applicable to datasets acquired through in vivo cortical imaging. (a) Experimental scheme of in vivo Ca^{2+} imaging through a cortical cranial window. (b) Astrocytic Ca^{2+} activity in the frontal cortex of a transgenic mouse expressing GCaMP3, represented as the average Ca^{2+} activity $\Delta F/F_0$ (left) and the fraction of active time (right) in the anesthetized and fully awake mouse. Scale bars = 20 µm. (c) Data for the Ca^{2+} event duration in anesthetized and awake mice summarized in 2D contour plots. (d) Frequency differences in Ca^{2+} event duration in anesthetized and awake mice. A gamma of 0.5 was applied to emphasize small changes in frequency. (e) Statistical evaluation of frequency differences in Ca^{2+} event duration from 1.5 to 7 s. Data show mean and SEM. Two-way ANOVA on arcsine transformed data with Sidak's multiple comparisons post-hoc test ($n = 10$ recordings from $N = 3$ mice in (c)–(e))

organization of the hippocampus is mostly preserved, and the maturation of different cell types, network connections, and receptor/channel expression are closer to the situation in vivo (Gähwiler et al., 1997; Gogolla et al., 2006). Figure 5(a),(b) show the average $\Delta F/F_0$ and the fraction of active time detected for the same preparation at 37 and 25°C. Notably, in organotypic slices, we obtained a similar temperature-dependence of astrocyte Ca^{2+} characteristics as in primary astrocyte cultures. At 37°C, the maximal Ca^{2+} levels were lower and events shorter and spatially more restricted, whereas at 25°C, astrocytes exhibited long-lasting Ca^{2+} events of lower frequency (Figure 5(c)). Detailed analysis of Ca^{2+} event duration in primary astrocyte cultures and organotypic hippocampal slices at 37°C revealed an additional set of long-lasting high-magnitude events in the latter preparations (areas in open red boxes, compare Figure 5(c) to Figure 3(c)). As the main difference between these two preparations is the absence of neurons in primary astrocytic cultures, we hypothesized that long-lasting Ca^{2+} events may be a consequence of neuronal activity. Supporting this hypothesis, we observed a similar Ca^{2+} activity pattern in astrocyte-neuron co-cultures (Supplementary Figure S5). To verify the impact of neurons in the hippocampal slice preparations, we blocked neuronal activity by applying tetrodotoxin (TTX; Figure 5 (d)). This treatment led to a pronounced reduction in long-lasting Ca^{2+} events in both organotypic preparations and astrocyte-neuron co-cultures, shifting Ca^{2+} activity to an event pattern observed in primary hippocampal astrocyte cultures at 37°C (Figure 5(e), Supplementary Figure S5). These findings demonstrate that the MTED algorithm can identify the impact of neuronal activity on astrocytic Ca^{2+} activity.

3.6 | Event detection in recordings obtained in vivo

To further investigate the versatility of the MTED approach, we evaluated astrocytic Ca^{2+} activity in vivo, for which the recorded fluorescence signal F is commonly much smaller, resulting in more challenging quantification of Ca^{2+} signals. To this end, we implanted a cortical cranial window into transgenic mice with astrocytic expression of GCaMP3 (Figure 6(a)). We set the excitation power between 30 and 40 mW to avoid light-induced Ca^{2+} activity and tissue damage, rarely detecting more than one photon per pixel and time point. Subsequently, we recorded and compared the Ca^{2+} activity patterns of the same cortical region in anesthetized and awake mice (Figure 6). Figure 6(b) depicts the average $\Delta F/F_0$ obtained, which coincides with the fraction of active time and shows overall low activity in the cortex of an anesthetized mouse. When the volatile anesthetic isoflurane was removed and mice woke up, the Ca^{2+} activity in the same region was drastically increased (Figure 6(b), Supplementary Figure S6 and Movie S6). Our analysis revealed that, compared to anesthetized conditions, awake mice had higher magnitude Ca^{2+} events and increased frequency of long-lasting events (Figure 6(c), Supplementary

Figure S6(c)–(e)). Figure 6(d) displays the differences in the Ca^{2+} activity pattern between anesthetized and awake conditions. Changes in frequency are most prominent at threshold levels 0.5 and 1 and for the subset of 1.5–7 s lasting events, which was supported by the statistical analysis (Figure 6(e)).

Overall, the Ca^{2+} activity in cortical astrocytes observed by in vivo imaging showed similar features in the Ca^{2+} pattern as obtained from cultured astrocytes measured at 37°C. The datasets further identify and define the impact of neuronal activity on a selective subset of Ca^{2+} characteristics of astrocytes (Figure 6(c) and Figure 5(d)). Importantly, the only necessary parameters for MTED of Ca^{2+} signals were the thresholds of F_0 and Ca^{2+}. More importantly, our approach robustly detected and comprehensively characterized Ca^{2+} event patterns not only in vitro and in situ but also in vivo.

4 | DISCUSSION

4.1 | Establishing a new event detection algorithm for analyzing astrocytic Ca^{2+} signals

With the development of fluorescent indicators of biological activities and metabolites, it has become possible to visualize structural activity and function on a subcellular level. Using GCaMP indicators to monitor the Ca^{2+} signals in astrocytes revealed the complexity of these processes, which cannot be described as on or off activity (i.e., below or above a particular threshold). Ca^{2+} event characterization in terms of magnitude, duration, propagation, regional connectivity, and correct event origin provides valuable information about this signaling pathway and is fundamental for understanding the functional role of Ca^{2+} activity in astrocytes.

During the past years, analysis of astrocyte Ca^{2+} activity has been continuously improved. Two examples of algorithms are CaSCaDe and AQuA (Agarwal et al., 2017; Wang et al., 2019), which use statistics-based data standardization techniques to estimate and remove the per-pixel fluorescence baseline. Such standardization, however, results in constant values, which does not permit to adapt to fluctuation in baseline fluorescence within the temporal evolution of a pixel. In contrast, MTED's F_0 estimation is able to adapt to these fluctuations and can thus compensate changes in fluorescence at basal levels of Ca^{2+} for the time-course of each individual pixel.

In addition, CaSCaDe uses classical, static ROIs to represent Ca^{2+} events. These are then analyzed and classified using a Support-vector machine (SVM), as a machine learning approach. AQuA extends the concept of static ROIs to so-called dynamic events, possessing the ability to adapt to morphological changes of a Ca^{2+} event on a per-frame basis. In both cases, detected ROIs are then subjected to further analysis.

In the present study, we further improve the flexibility of analysis by developing the MTED algorithm, a novel event detection strategy for time-lapse data obtained by fluorescence microscopy. It is pixel-based and uses multiple thresholds. We chose the latter because signal-to-noise-based strategies for detection of events are prone to underestimating activity in regions with low fluorescence intensity (e.g., low indicator concentrations). This can lead to missed events because the signaling amplitudes stay below a single threshold. The multi-threshold approach developed here overcomes this problem. We applied our analysis to data of astrocytic Ca^{2+} signaling as a test case. It enabled us to quantitatively analyze multiple aspects of Ca^{2+} event patterns that evolve in time and space. Indeed, the approach maintained its robustness when weak signals from small astrocytic processes in more intact preparations were analyzed. Characterization of such weak signals is important because those processes are in close proximity with the extracellular matrix, surrounding cells, and synapses, and also represent the origin of the majority of Ca^{2+} events in astrocytes (Bindocci et al., 2017; Wu et al., 2019). This robustness is also important for other fluorescent indicators that do not display the large fluorescence changes of modern Ca^{2+} indicators, such as many FRET-based sensors.

For all indicators, the relationship between indicator fluorescence and ligand concentration requires careful assessment. In many cases, this relationship is non-linear, and it needs careful consideration to what extent this affects the interpretation of the results. In our study, we used a common measure of fluorescence intensity and its changes ($\Delta F/F_0$). While this quantification has its drawbacks, see for instance (Semyanov et al., 2020), it is straight-forward and abundantly used throughout biomedical research and therefore suitable for testing the analytical approach and its versatility. Since the MTED algorithm is oblivious to the type of data it is working on and does not make specific assumption about it, it can be fed with more quantitative data (e.g., $[Ca^{2+}]$ after calibration of the imaging setup). Furthermore, it is not limited to Ca^{2+} signaling and could be applied to various fluorescent indicator families and readouts.

In this study we used only a fraction of parameters provided by MTED (compare Figure S3) which are already rather complex due to their multi-dimensionality. Further reduction of complexity can be achieved by applying dimensionality-reducing approaches such as principal component analysis, as recently suggested by Vaidyanathan et. al (Vaidyanathan et al., 2021). Depending on the scientific question those data could be also further examined with cluster analysis strategies such as k-Means.

4.2 | Temperature-dependence of Ca^{2+} signaling in astrocytes

Comparing the Ca^{2+} event detection strategies, some predominately describe only fast and regionally restricted event spots, from which they conclude that discussing frequency patterns in restricted active regions is sufficient for the characterization of astrocytic Ca^{2+} activity (Agarwal et al., 2017; Wang et al., 2017). Other approaches identify a substantial fraction of long-lasting events with regional growth and overlapping patterns, which require the analysis of dynamic regions (Wang et al., 2019; Wu et al., 2019). Here, we observed both types; when examining Ca^{2+} activity at physiological temperature (i.e., 37°C),

we observed the first, whereas imaging the same region at RT led to observation of the latter scenario. Our MTED algorithm sufficiently describes both states of this reversible behavior. We revealed that changes in Ca^{2+} event patterns rely on changes in Ca^{2+} clearance from the cytosol, which is temperature-dependent (Arrhenius, 1889; Komin et al., 2015; Schipper et al., 2014). A relatively straight-forward explanation is that when the Ca^{2+} uptake is slowed down, Ca^{2+} diffuses to larger volumes, accumulates, and initiates Ca^{2+}-induced Ca^{2+} release leading to high magnitude Ca^{2+} transients. Blocking the Ca^{2+} uptake by CPA at 37°C indeed switched the Ca^{2+} activity profile to the patterns obtained at 25°C. Remarkably, minor deviations from the species-dependent physiological temperature, such as cooling to 34°C (a temperature typically used in patch-clamp experiments), cause prominent aberrations in the characteristics of Ca^{2+} activity.

Our observation of the temperature-dependent Ca^{2+} activity has broad consequences for interpreting published findings, as well as for future experimental designs. Deviations between astrocytic Ca^{2+} behavior obtained in vitro, in situ, and in vivo may be partly explained by different environmental conditions: 25°C for primary cultures, 34°C for organotypic slices, and 37°C for in vivo measurements. More importantly, Ca^{2+} activity patterns obtained in our ex vivo experiments at 37°C were similar to those in vivo. The dissection of the temperature dependence of astrocytic Ca^{2+} signaling demonstrates that our analytical approach can be used to compare experimental results across preparations and experimental conditions.

4.3 | Cellular environment and state of consciousness shape Ca^{2+} signals in astrocytes

As a second test scenario, we explored how astrocytic Ca^{2+} event patterns are shaped by neuronal activity. We found, for instance, that the occurrence of long-lasting events can be reduced by blocking action potentials in organotypic slices and mixed cultures of astrocytes and neurons with the application of TTX. This adds to previous studies on how neuronal activity modifies astrocytic Ca^{2+} signaling (Bazargani & Attwell, 2016), by identifying the subset of Ca^{2+} events that is impacted. The obtained results suggest that the connectivity between co-cultured neurons and astrocytes is not as dense as in organotypic slice cultures (compare Figure 5(d),(e) and Supplementary Figure S5). An advantage of the presented analysis is the simpler visualization and identification of groups of events that depend on a specific experimental condition, in our example the presence of neurons/neuronal activity. Furthermore, the location and time of this special group of long-lasting Ca^{2+} events can be identified and could potentially be correlated with nearby neuronal structures. More generally, this approach may help with associating spatiotemporal patterns and properties of cellular events reported by fluorescence with biologically relevant mechanisms and conditions.

As a first step toward the latter, we analyzed Ca^{2+} transients of anesthetized and awake animals. Doing so confirmed that Ca^{2+} activity in astrocytes is reduced under anesthetized conditions (Bojarskaite et al., 2020; Thrane et al., 2012; Vaidyanathan et al., 2021). Interestingly, this is partly because of a reduction of pronounced Ca^{2+} events with large magnitude whereas the frequency of small magnitude events did not significantly change: an important distinction and refinement. This is a third example of how the MTED analysis can extract important additional information from time-lapse fluorescence microscopy, a type of data set ubiquitous in neurobiology and beyond.

ACKNOWLEDGMENTS

This study was supported by the German Research Foundation (DFG) grant PO732 (EGP), German Research Foundation (DFG) grant ZE994/2 (AZ), German Research Foundation (DFG) grant SFB1089 B03, SPP1757, HE6949/1 and HE6949/3(CH), German Research Foundation (DFG) grant SFB 894 A12, SPP 1757 KI 503/12-2 (FK), and European Union's Horizon 2020 Research and Innovation Program grant 722053 (LCC). Open Access funding enabled and organized by Projekt DEAL.

CONFLICT OF INTERESTS

The authors declare no competing interests.

AUTHOR CONTRIBUTIONS

Conceptualization: Andre Zeug, Volodymyr Cherkas, Gebhard Stopper. Methodology: Andre Zeug, Volodymyr Cherkas, Gebhard Stopper. Investigation: Franziska E. Müller, Volodymyr Cherkas, Gebhard Stopper, Laura Stopper, Laura C. Caudal. Visualization: Franziska E. Müller, Andre Zeug. Supervision: Evgeni G. Ponimaskin, Frank Kirchhoff, Christian Henneberger. Writing–original draft: Franziska E. Müller, Andre Zeug. Writing–review & editing: Franziska E. Müller, Volodymyr Cherkas, Gebhard Stopper, Laura C. Caudal, Laura Stopper, Frank Kirchhoff, Christian Henneberger, Evgeni G. Ponimaskin, Andre Zeug. This manuscript is part of the PhD thesis of Franziska E. Müller.

DATA AVAILABILITY STATEMENT

The Matlab code developed in this study is available from the corresponding author upon request.

ORCID

Franziska E. Müller https://orcid.org/0000-0003-0525-0714
Gebhard Stopper https://orcid.org/0000-0003-2496-4755
Laura C. Caudal https://orcid.org/0000-0003-2165-281X
Laura Stopper https://orcid.org/0000-0002-9648-6222
Frank Kirchhoff https://orcid.org/0000-0002-2324-2761
Christian Henneberger https://orcid.org/0000-0002-5391-7387
Evgeni G. Ponimaskin https://orcid.org/0000-0002-4570-5130
Andre Zeug https://orcid.org/0000-0001-9858-5841

REFERENCES

Agarwal, A., Wu, P.-H., Hughes, E. G., Fukaya, M., Tischfield, M. A., Langseth, A. J., Wirtz, D., & Bergles, D. E. (2017). Transient Opening of the Mitochondrial Permeability Transition Pore Induces Microdomain Calcium Transients in Astrocyte Processes. *Neuron*, *93*(3), 587–605. e7. https://doi.org/10.1016/j.neuron.2016.12.034

Araque, A., Carmignoto, G., Haydon, P. G., Oliet, S. H. R., Robitaille, R., & Volterra, A. (2014). Gliotransmitters Travel in Time and Space. *Neuron*, *81*(4), 728–739. https://doi.org/10.1016/j.neuron.2014.02.007

Arrhenius, S. (1889). Über die reaktionsgeschwindigkeit bei der inversion von rohrzucker durch säuren. *Zeitschrift für Physikalische Chemie*, *4U*(1), 226–248. https://doi.org/10.1515/zpch-1889-0416

Bazargani, N., & Attwell, D. (2016). Astrocyte calcium signaling: The third wave. *Nature Neuroscience*, *19*(2), 182–189. https://doi.org/10.1038/nn.4201

Bindocci, E., Savtchouk, I., Liaudet, N., Becker, D., Carriero, G., & Volterra, A. (2017). Three-dimensional Ca2+ imaging advances understanding of astrocyte biology. *Science*, *356*(6339), eaai8185. https://doi.org/10.1126/science.aai8185

Bojarskaite, L., Bjørnstad, D. M., Pettersen, K. H., Cunen, C., Hermansen, G. H., Åbjørsbråten, K. S., Chambers, A. R., Sprengel, R., Vervaeke, K., Tang, W., Enger, R., & Nagelhus, E. A. (2020). Astrocytic Ca 2+ signaling is reduced during sleep and is involved in the regulation of slow wave sleep. *Nature Communications*, *11*(1), 3240. https://doi.org/10.1038/s41467-020-17062-2

Bonansco, C., Couve, A., Perea, G., Ferradas, C. Á., Roncagliolo, M., & Fuenzalida, M. (2011). Glutamate released spontaneously from astrocytes sets the threshold for synaptic plasticity. *European Journal of Neuroscience*, *33*(8), 1483–1492. https://doi.org/10.1111/j.1460-9568.2011.07631.x

Castro, M. A. D., Chuquet, J., Liaudet, N., Bhaukaurally, K., Santello, M., Bouvier, D., Tiret, P., & Volterra, A. (2011). Local Ca 2+ detection and modulation of synaptic release by astrocytes. *Nature Neuroscience*, *14*(10), 1276–1284. https://doi.org/10.1038/nn.2929

Chai, H., Diaz-Castro, B., Shigetomi, E., Monte, E., Octeau, J. C., Yu, X., Cohn, W., Rajendran, P. S., Vondriska, T. M., Whitelegge, J. P., Coppola, G., & Khakh, B. S. (2017). Neural circuit-specialized astrocytes: Transcriptomic, proteomic, morphological and functional evidence. *Neuron*, *95*(3), 531–549.e9. https://doi.org/10.1016/j.neuron.2017.06.029

Chen, T.-W., Wardill, T. J., Sun, Y., Pulver, S. R., Renninger, S. L., Baohan, A., Schreiter, E. R., Kerr, R. A., Orger, M. B., Jayaraman, V., Looger, L. L., Svoboda, K., & Kim, D. S. (2013). Ultrasensitive fluorescent proteins for imaging neuronal activity. *Nature*, *499*(7458), 295–300. https://doi.org/10.1038/nature12354

Cupido, A., Cătălin, B., Steffens, H., & Kirchhoff, F. (2014). *Surgical procedures to study microglial motility in the brain and in the spinal cord by in vivo two-photon laser-scanning microscopy*. Springer. https://experiments.springernature.com/articles/10.1007/978-1-4939-0381-8_2

Gähwiler, B. H., Capogna, M., Debanne, D., McKinney, R. A., & Thompson, S. M. (1997). Organotypic slice cultures: A technique has come of age. *Trends in Neurosciences*, *20*(10), 471–477. https://doi.org/10.1016/s0166-2236(97)01122-3

Gogolla, N., Galimberti, I., DePaola, V., & Caroni, P. (2006). Long-term live imaging of neuronal circuits in organotypic hippocampal slice cultures. *Nature Protocols*, *1*(3), 1223–1226. https://doi.org/10.1038/nprot.2006.169

Guo, Z. V., Hires, S. A., Li, N., O'Connor, D. H., Komiyama, T., Ophir, E., Huber, D., Bonardi, C., Morandell, K., Gutnisky, D., Peron, S., Xu, N., Cox, J., & Svoboda, K. (2014). Procedures for behavioral experiments in head-fixed mice. *PLoS ONE*, *9*(2), e88678. https://doi.org/10.1371/journal.pone.0088678

Henneberger, C., Papouin, T., Oliet, S. H. R., & Rusakov, D. A. (2010). Long term potentiation depends on release of D-serine from astrocytes. *Nature*, *463*(7278), 232–236. https://doi.org/10.1038/nature08673

Horikawa, K. (2015). Recent progress in the development of genetically encoded Ca2+ indicators. *The Journal of Medical Investigation: JMI*, *62*(1–2), 24–28. https://doi.org/10.2152/jmi.62.24

Kislin, M., Mugantseva, E., Molotkov, D., Kulesskaya, N., Khirug, S., Kirilkin, I., Pryazhnikov, E., Kolikova, J., Toptunov, D., Yuryev, M., Giniatullin, R., Voikar, V., Rivera, C., Rauvala, H., & Khiroug, L. (2014). Flat-floored air-lifted platform: A new method for combining behavior with microscopy or electrophysiology on awake freely moving rodents. *Journal of Visualized Experiments: JoVE*, *88*, e51869. https://doi.org/10.3791/51869

Kobe, F., Guseva, D., Jensen, T. P., Wirth, A., Renner, U., Hess, D., Müller, M., Medrihan, L., Zhang, W., Zhang, M., Braun, K., Westerholz, S., Herzog, A., Radyushkin, K., El-Kordi, A., Ehrenreich, H., Richter, D. W., Rusakov, D. A., & Ponimaskin, E. (2012). 5-HT7R/G12 Signaling Regulates Neuronal Morphology and Function in an Age-Dependent Manner. *The Journal of Neuroscience*, *32*(9), 2915–2930. https://doi.org/10.1523/JNEUROSCI.2765-11.2012

Komin, N., Moein, M., Ellisman, M. H., & Skupin, A. (2015). *Multiscale Modeling Indicates That Temperature Dependent [Ca2]* [Research article]. *Neural Plasticity*, *2015*, 1–15. https://doi.org/10.1155/2015/683490

Maggioni, M., Boracchi, G., Foi, A., & Egiazarian, K. (2012). Video Denoising, Deblocking, and Enhancement Through Separable 4-D Nonlocal Spatiotemporal Transforms. *IEEE Transactions on Image Processing*, *21*(9), 3952–3966. https://doi.org/10.1109/TIP.2012.2199324

Meldolesi, J. (2004). The development of Ca2+ indicators: A breakthrough in pharmacological research. *Trends in Pharmacological Sciences*, *25*(4), 172–174. https://doi.org/10.1016/j.tips.2004.02.004

Mori, T., Tanaka, K., Buffo, A., Wurst, W., Kühn, R., & Götz, M. (2006). Inducible gene deletion in astroglia and radial glia—A valuable tool for functional and lineage analysis. *Glia*, *54*(1), 21–34. https://doi.org/10.1002/glia.20350

Nett, W. J., Oloff, S. H., & McCarthy, K. D. (2002). Hippocampal Astrocytes In Situ Exhibit Calcium Oscillations That Occur Independent of Neuronal Activity. *Journal of Neurophysiology*, *87*(1), 528–537. https://doi.org/10.1152/jn.00268.2001

Panatier, A., Vallée, J., Haber, M., Murai, K. K., Lacaille, J.-C., & Robitaille, R. (2011). Astrocytes Are Endogenous Regulators of Basal Transmission at Central Synapses. *Cell*, *146*(5), 785–798. https://doi.org/10.1016/j.cell.2011.07.022

Paukert, M., Agarwal, A., Cha, J., Doze, V. A., Kang, J. U., & Bergles, D. E. (2014). Norepinephrine controls astroglial responsiveness to local circuit activity. *Neuron*, *82*(6), 1263–1270. https://doi.org/10.1016/j.neuron.2014.04.038

Pérez Koldenkova, V., & Nagai, T. (2013). Genetically encoded Ca2+ indicators: Properties and evaluation. *Biochimica et Biophysica Acta (BBA) - Molecular Cell Research*, *1833*(7), 1787–1797. https://doi.org/10.1016/j.bbamcr.2013.01.011

Pologruto, T. A., Sabatini, B. L., & Svoboda, K. (2003). ScanImage: Flexible software for operating laser scanning microscopes. *Biomedical Engineering Online*, *2*, 13. https://doi.org/10.1186/1475-925X-2-13

Porter, J. T., & Mccarthy, K. D. (1997). Astrocytic neurotransmitter receptors in situ and in vivo. *Progress in Neurobiology*, *51*(4), 439–455. https://doi.org/10.1016/S0301-0082(96)00068-8

Schipper, L. A., Hobbs, J. K., Rutledge, S., & Arcus, V. L. (2014). Thermodynamic theory explains the temperature optima of soil microbial processes and high Q10 values at low temperatures. *Global Change Biology*, *20*(11), 3578–3586. https://doi.org/10.1111/gcb.12596

Semyanov, A., Henneberger, C., & Agarwal, A. (2020). Making sense of astrocytic calcium signals—From acquisition to interpretation. *Nature Reviews Neuroscience*, *21*(10), 551–564. https://doi.org/10.1038/s41583-020-0361-8

Sofroniew, M. V., & Vinters, H. V. (2010). Astrocytes: Biology and pathology. *Acta Neuropathologica*, *119*(1), 7–35. https://doi.org/10.1007/s00401-009-0619-8

Thrane, A. S., Rangroo Thrane, V., Zeppenfeld, D., Lou, N., Xu, Q., Nagelhus, E. A., & Nedergaard, M. (2012). General anesthesia selectively disrupts astrocyte calcium signaling in the awake mouse cortex. *Proceedings of the National Academy of Sciences*, *109*(46), 18974–18979. https://doi.org/10.1073/pnas.1209448109

Vaidyanathan, T. V., Collard, M., Yokoyama, S., Reitman, M. E., & Poskanzer, K. E. (2021). Cortical astrocytes independently regulate

sleep depth and duration via separate GPCR pathways. *eLife*, *10*, e63329. https://doi.org/10.7554/eLife.63329

Venugopal, S., Srinivasan, R., & Khakh, B. S. (2019). GECIquant: Semi-automated Detection and Quantification of Astrocyte Intracellular Ca2+ Signals Monitored with GCaMP6f. In M. De Pittà & H. Berry (Eds.), *Computational Glioscience (S. 455–470)*. Springer International Publishing. https://doi.org/10.1007/978-3-030-00817-8_17

Volterra, A., Liaudet, N., & Savtchouk, I. (2014). Astrocyte Ca2+ signalling: An unexpected complexity. *Nature Reviews Neuroscience*, *15*(5), 327–335. https://doi.org/10.1038/nrn3725

Volterra, A., & Meldolesi, J. (2005). Astrocytes, from brain glue to communication elements: The revolution continues. *Nature Reviews Neuroscience*, *6*(8), 626–640. https://doi.org/10.1038/nrn1722

Wang, Y., DelRosso, N. V., Vaidyanathan, T. V., Cahill, M. K., Reitman, M. E., Pittolo, S., Mi, X., Yu, G., & Poskanzer, K. E. (2019). Accurate quantification of astrocyte and neurotransmitter fluorescence dynamics for single-cell and population-level physiology. *Nature Neuroscience*, *22*(11), 1936–1944. https://doi.org/10.1038/s41593-019-0492-2

Wang, Y., Shi, G., Miller, D. J., Wang, Y., Wang, C., Broussard, G., Wang, Y., Tian, L., & Yu, G. (2017). Automated Functional Analysis of Astrocytes from Chronic Time-Lapse Calcium Imaging Data. *Frontiers in Neuroinformatics*, *11*, 1–23. https://doi.org/10.3389/fninf.2017.00048

Wu, Y.-W., Gordleeva, S., Tang, X., Shih, P.-Y., Dembitskaya, Y., & Semyanov, A. (2019). Morphological profile determines the frequency of spontaneous calcium events in astrocytic processes. *Glia*, *67*(2), 246–262. https://doi.org/10.1002/glia.23537

Wu, Y.-W., Tang, X., Arizono, M., Bannai, H., Shih, P.-Y., Dembitskaya, Y., Kazantsev, V., Tanaka, M., Itohara, S., Mikoshiba, K., & Semyanov, A. (2014). Spatiotemporal calcium dynamics in single astrocytes and its modulation by neuronal activity. *Cell Calcium*, *55*(2), 119–129. https://doi.org/10.1016/j.ceca.2013.12.006

SUPPORTING INFORMATION

Additional supporting information may be found online in the Supporting Information section at the end of this article.

How to cite this article: Müller, F. E., Cherkas, V., Stopper, G., Caudal, L. C., Stopper, L., Kirchhoff, F., Henneberger, C., Ponimaskin, E. G., & Zeug, A. (2021). Elucidating regulators of astrocytic Ca^{2+} signaling via multi-threshold event detection (MTED). *Glia*, *69*(12), 2798–2811. https://doi.org/10.1002/glia.24070